Journal Pre-proof

Local Field Potential Journey into the Basal Ganglia

Shay Moshel, Eitan E. Asher, Maya Slovik, Rea Mitelman, Hagai Bergman, Shlomo Havlin

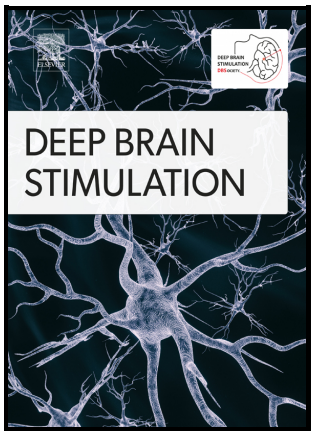

PII: S2949-6691(24)00004-6

DOI: https://doi.org/10.1016/j.jdbs.2024.03.002

Reference: JDBS25

To appear in: *Deep Brain Stimulation*

Received date: 3 August 2023
Revised date: 29 February 2024
Accepted date: 19 March 2024

Please cite this article as: Shay Moshel, Eitan E. Asher, Maya Slovik, Rea Mitelman, Hagai Bergman and Shlomo Havlin, Local Field Potential Journey into the Basal Ganglia, *Deep Brain Stimulation,* (2024) doi:https://doi.org/10.1016/j.jdbs.2024.03.002

Local Field Potential Journey into the Basal Ganglia

Shay Moshel[1,2,3,4], Eitan E. Asher[1], Maya Slovik[2,3], Rea Mitelman[2,3], Hagai Bergman[2,3], Shlomo Havlin[1]

[1]Department of Physics, Bar-Ilan University, Ramat Gan, Israel
[2]Department of Medical Neurobiology, The Hebrew University-Hadassah Medical School, Jerusalem, Israel
[3] The Edmond and Lily Safra Center for Brain Sciences, The Hebrew University, Jerusalem, Israel
[4] Nuclear Research Center Negev, Beer-Sheva, Israel

E-mail: shaymoshel@gmail.com

Abstract. Local field potentials (LFP) in the basal ganglia (BG) have attracted considerable research and clinical interest. The genesis of these signals has been a topic of extensive discourse, focusing on whether they are a manifestation of local synaptic activity or result from the propagation of electrical signals through tissue, as described by the Maxwell equations (volume conduction). To investigate this, we conducted simultaneous recordings of LFPs from two cortical areas— the dorsolateral prefrontal cortex (DLPFC) and the primary motor cortex (M1)—and various sites within the BG nuclei in an awake, non-task-engaged non-human primate (NHP). Employing innovative analytical techniques, we discerned significant cross-correlations indicative of potential connections, while filtering out non-significant correlations. This allowed us to differentiate between synaptic inputs and volume conduction. Our findings indicate two distinct propagation pathways of BG field potentials emanating from the M1 and the DLPFC, each characterized by different temporal delays. The results imply that these anatomical pathways are differentially influenced by the mechanisms of volume conduction and synaptic transmission. Notably, the M1 exhibits more functional links with non-zero-time delays to the BG structures, while the DLPFC-BG connections are marked by zero-time delays, suggesting a predominance of volume conduction effects. Consequently, investigations into the origins of BG LFP should account for the distinct anatomical pathways linking the cortex and the BG, as they differentially represent information flow and volume conductance.

Keywords: Basal Ganglia (BG), Cerebral Cortex (CTX), Local Field Potential (LFP), Volume Conduction, Synaptic Input, Cross Correlation

‡

1. Introduction

The study of broadband field potentials is pivotal in advancing our understanding of neuronal functions, identifying pathological aberrations, and observing clinical phenomena. Behavioral research has utilized local field potential (LFP) activity as a biomarker for cognitive processes [1–3] and as a response indicator to sensory stimuli [4–6]. The development of brain-machine interfaces has further capitalized on the insights gleaned from LFPs [7] and electroencephalogram (EEG) [8] signals. Correlations between LFPs in the subthalamic nucleus and cortical somatosensory-related EEGs [9], as well as associations between neural discharge rates and LFP signals in the cerebral cortex during voluntary actions [10], exemplify the diverse applications of LFPs. Furthermore, the increase in abnormal LFP oscillations in the basal ganglia (BG) and cerebral cortex is a hallmark of neurological disorders like Parkinson's disease (PD) and schizophrenia [11–13].

The LFP frequency spectrum typically spans from 0.1 to 70 Hz, with oscillations above 100 Hz classified as high-frequency LFP oscillations [14], which may be confounded by the transference of spike energy [15]. Despite the common belief that LFP oscillations suggest spike synchronization [12, 16–18], it is increasingly evident that these signals may instead signify sub-threshold synaptic activities, potentially in tandem with spike activity [1, 19]. Broadband field potentials have also demonstrated partial correlations with spontaneous cerebral low-frequency BOLD signal fluctuations [20, 21]. Hermes et al. [21] posited that the characteristics of field potentials that are uncorrelated with BOLD signals primarily originate from changes in neuronal synchrony, as opposed to direct neuronal activity levels.

While broadband field potentials are integral to brain behavior analysis and relatively straightforward to record, the origins of LFP remain contentious. Numerous studies advocate that LFPs embody crucial neuronal information stemming from local synaptic activities [16, 22–25]. Alternatively, some research presents these signals, especially when sourced from subcortical structures, as propagative electromagnetic waves that comply with the principles of volume conduction according to Maxwell's equations [21, 26–28]. For example, Parabucki et al. [27] observed robust LFP coupling during whisker stimulation between the cerebral cortex and the olfactory bulb in mice with a dissected olfactory bulb. Lalla et al. [29] investigated LFP oscillations and spike activity recorded simultaneously in the dorsolateral striatum (DLS) and the forelimb primary somatosensory cortex (S1) of rats, detecting signs of a shared extrinsic source for the LFP signals in both regions. Yet, Buzsaki et al. [1] argue for a hybrid nature of LFP signals, incorporating elements of both volume conduction and localized extracellular fields.

Despite substantial research, a definitive understanding of the genesis of broadband field

‡ **Abbreviations:** Basal Ganglia (BG), Cerebral Cortex (CTX), Primary Motor Cortex (M1), Dorsolateral Prefrontal Cortex (DLPFC), Striatum (STR), Globus Pallidus (GP), Internal Capsule (IC), Subthalamic Nucleus (STN), Local Field Potential (LFP), Non-Human Primates (NHP), Deep Brain Stimulation (DBS)

potentials remains elusive. Are they volume-conducted electromagnetic waves disseminating within the brain's deeper strata, or do they transmit valuable information such as synaptic inputs? Moreover, if representing an intermediate phenomenon, it becomes critical to determine the relative contributions of volume conduction and synaptic inputs, and to ascertain whether these contributions are prolonged, continuous, or occur in brief durations interspersed within the same recording sites. To address these questions, we map LFPs from the cerebral cortex through the basal ganglia nuclei in non-human primates (NHPs).

We employed micro-electrodes to record the comprehensive electrophysiological spectrum (raw data) across a frequency range of [1, 6000] Hz. Between 1 to 7 electrodes were steadfastly positioned in the deep cortical layers throughout all recording sessions, as depicted in Fig.1(A). An additional electrode was maneuvered towards the BG nuclei. The neural activity from all electrodes was concurrently captured every 200 μm over a duration of 120 seconds, beginning with the insertion of the eighth electrode into the cerebral cortex (frontal lobe) and traversing through the striatum, globus pallidus (external - GPe, internal - GPi), internal capsule, and the subthalamic nucleus. We isolated the LFP signal by filtering the raw data within the frequency range of 1-80Hz. Recordings were monopolar, using a common reference point located at the posterior aspect of the NHP's cranium. These concurrent LFP recordings were scrutinized to elucidate the interplay between neuronal activities in the cerebral cortex and the deep strata of the BG.

2. Methods

2.1. Animals, surgery and MRI

This study was conducted on a single African Green monkey (Cercopithecus aethiops, female, 3.3 kg). The experimental protocols adhered to the ethical guidelines set by the Hebrew University and conformed to the National Institutes of Health Guide for the Care and Use of Laboratory Animals. The institution holds accreditation from the Association for Assessment and Accreditation of Laboratory Animal Care (AAALAC).

Prior to experimentation, the monkey was acclimatized to remain calmly seated in a primate chair. Subsequent to this behavioral training, the subject underwent a surgical procedure to implant a Cylux MRI-compatible recording chamber (27*27 mm, Alpha-Omega, Israel) and a head holder (Crist Instruments, MD). The chamber's placement was guided by coordinates from established primate stereotaxic atlases [30, 31], targeting the region above the right primary motor cortex (M1), globus pallidus (Gp), and the subthalamic nucleus (Stn). A postoperative MRI scan was performed to confirm the precise stereotaxic coordinates of the implant.

2.2. Recording and data acquisition

During the recording sessions, the primate was positioned in a specialized chair, designed to restrict movement of the head and hands while allowing the trunk and legs freedom of movement. This

setup ensured the animal remained in a state of quiet alertness throughout the process. The precise locations for data recording were ascertained individually for each targeted structure. The primary motor cortex (M1) was confirmed via the motor response of the limbs to electrical stimulation ranging from 10 to 40 μA. The dorsolateral prefrontal cortex (DLPFC) was identified by its anatomical placement within the surgical chamber.

The basal ganglia (BG) nuclei complex, consisting of the striatum, globus pallidus, and the subthalamic nucleus, were differentiated based on distinct physiological characteristics. Additionally, the subthalamic nucleus was specifically validated through the cellular response to passive limb movement. The recorded extracellular data were amplified with a gain of 5000x and band-pass filtered between 1 to 6000 Hz using a four-pole Butterworth filter. This data was then continuously sampled at a rate of 25 kHz.

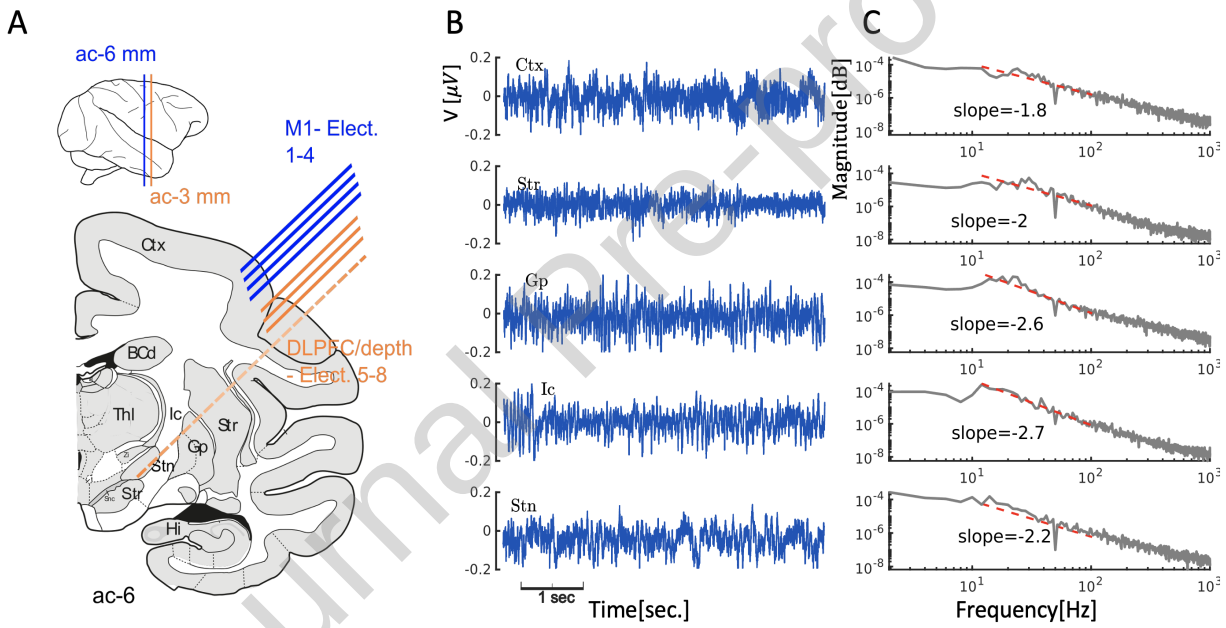

Figure 1: **Anatomical and electrodes setup, raw data and power spectrum densities. A,** Hemi-coronal illustration from Macaque atlas, at the level of anterior commissure (AC) - 6 mm. We placed 7 electrodes in the deep layers of the cerebral cortex. Electrodes 1-4 (M1) were permanently located on the right–hemisphere, primary M1- motor-cortex, and electrodes 5-7 (DLPFC) on the right hemisphere – dorso-lateral frontal cortex. One electrode aimed to the basal ganglia, passing through the recording sites in: the cerebral cortex (Ctx), striatum (Str), globus pallidus (Gp) internal capsule (Ic) and subthalamic nucleus (Stn). Each site has been recorded for time duration of 120 seconds. Labels in cartoon: A to F mark the recorded area. **B,** Examples of 5 seconds records of raw local field potential data from shallow to deep loci: Ctx, Str, Gp, Ic and Stn, and **C,** The corresponding power spectral density, after applying a notch filter to remove the 50Hz band.

2.3. Electrode Arrays and Positioning

For the recordings, we employed two arrays each containing four glass-coated tungsten microelectrodes (impedance at 1 kHz, ranging from 0.2-0.6 MOhm), housed within a cylindrical metal guide with an internal diameter of 1.36 mm. The first array of electrodes (M1 electrodes) was strategically placed in the primary motor cortex area, while the remaining electrodes (E5-7) were anchored in the frontal cortex, and electrode E8 was targeted at the basal ganglia nuclei, as illustrated in Fig.1(A). Precise electrode placement was facilitated by the double Microdriving Terminal and Electrode Positioning System (Double MT and EPS, Alpha-Omega, Israel), which allows for the independent adjustment of each electrode.

Our database encompasses 13 distinct and non-repeating trajectories within the basal ganglia nuclei, each directed to specific locations within the Basal Ganglia, predominantly targeting the globus pallidus (Gp) and subthalamic nucleus (Stn). Target coordinates were derived from a composite method of indirect targeting, based on the anterior commissure-posterior commissure line using aMonkey atlas, which had been approved based on previous trajectory assessments for target locations. Furthermore, post-surgery MRI-based assessments were also utilized to confirm the accuracy of the target locations.

The verification of recording locations (Str, GPi, GPe, IC, and Stn) was meticulously conducted for each nucleus according to its specific electro-physiological spectrum patterns, aiding in their identification: (i). Striatum (STR): Characterized by specific firing rates, we focused on identifying Medium-sized spiny neurons (MSN) and Tonic active neurons (TAN) cells within the STR. (ii). Globus Pallidus Externus (GPe) and Internus (GPi): The GPe was identified by its high-frequency discharge pattern with interspersed pauses, while the GPi was recognized by its continuous firing pattern without pauses. In this work, we decide to present GPe /Gpi as the whole GP. (iii). Internal Capsule (Ic): The Ic was distinguished based on the high-amplitude fiber firing rates. (iv). Subthalamic Nucleus (Stn): Known for its broad spectrum of firing rates and amplitudes, the Stn, especially its dorsolateral region, was identified by inducing limb movements in the animal subject to observe electrophysiological responses. Upon entering the Stn, specifically in the dorsolateral region and after achieving a stable signal, one of the experimenters entered the animal room to manipulate the animal's limbs, inducing electrophysiological responses for further observation.

During the recording phase, electrodes E1-7 were fixed in the deep layers of the cerebral cortex, encompassing M1 and the frontal cortex above the basal ganglia, while the eighth electrode was progressively advanced towards the basal ganglia nuclei (Fig. 1A). We commenced simultaneous recordings from the cortical electrodes (E1-7) as soon as the mobile electrode penetrated the cerebral cortex. Each recording site was monitored for a duration of two minutes, following a brief period for signal stabilization. Upon completion of the recording at a given site, we proceeded to advance the mobile electrode by 200 μm to the next deeper location.

Location	Ctx	Str	Gp	Ic	Stn
Sites	210	219	91	20	18
Pairs	1318	1331	561	140	126

Table 1: **Data Summary.** The table displays the count of recording sites within each neural structure and the total number of pairings between cortical electrodes and the deep electrode. The deep electrode (E8) was advanced in steps of 200 μm from the cortex into the BG. Each distinct position sampled is defined as a site. At each site, signals from the deep electrode were cross-correlated with corresponding records from cortical electrodes E1-7, yielding the total pairings. Abbreviations: Ctx - cortex, Str - striatum, Gp - globus pallidus, Ic - internal capsule, Stn - subthalamic nucleus.

2.4. Data Analysis

Our analysis was conducted using Python 3.6 and MATLAB19a (R2019a) scripts. The database encompasses 13 distinct and non-repeating trajectories, extracted from the basal ganglia nuclei.

Throughout the recording sessions, the animal's behavior and the electrophysiological signals were continuously monitored via an online camera and sound amplifier. We systematically excluded data segments that included jaw and limb movements to prevent potential artifacts from affecting the analysis. In the offline preprocessing stage, we implemented several strategies to refine the quality of the LFP data and mitigate artifacts. This included the application of a low-pass filter and a notch filter, local averaging removal over 2.5-second intervals, and detrending to prepare the signals for subsequent analysis.

Specifically, a dual-stage filtration approach was applied to the preprocessing of LFP signals. Initially, a 15th-order zero-phase Butterworth band-stop filter was employed to attenuate the 50 Hz power-grid noise, selected for its flat frequency response which is crucial to preserve the integrity of the signal within the frequency range of interest. This step effectively removed the line noise without introducing phase shifts.

After the band-stop filter, we performed a DC offset correction on each LFP segment by subtracting the mean, yielding a zero-centered signal conducive to accurate frequency-domain analysis. We then applied a low-pass filter (Butterworth, 4 poles, within the range of [0-80] Hz) via frequency-domain manipulation. A Fast Fourier Transform (FFT) was applied to each centered signal segment, nullifying amplitudes outside the specified frequency band to attenuate higher frequencies. An inverse FFT of the modified spectrum provided us with a signal constrained to the desired frequency range, thereby eliminating high-frequency noise. This thorough preprocessing regimen, which included detrending, band-stop filtering, and low-pass filtering, prepared the LFP signals for the cross-correlation analysis devoid of electrical noise, DC offsets, and unwanted frequency components.

A summary of the data records, post these preprocessing steps, is presented in Table 1.

2.5. Cross-correlation and surrogate analysis to identify significant interactions

To quantify the similarities between two signals—specifically, those recorded from the cerebral cortex electrodes (E1-7) and basal ganglia (BG) sites (E8)—we employed cross-correlation analysis, as depicted in Figs. 2-3. Both signals, denoted as x and y, were segmented into N_L overlapping portions ν, each of length L=2.5 seconds, with an overlap of 0.625 seconds (L/4). This segmentation resulted in 63 time windows for each 120-second recording.

Each segment ν was normalized by subtracting its mean, ensuring that the analysis predominantly reflects fluctuations from the average. We then computed the cross-correlation function $R^{\nu}_{xy}(\tau) = \sum_{\tau=-n/2}^{n/2} x^{\nu}(n+\tau) * y^{\nu}(n)$ for each segment.

To differentiate between significant and non-significant interactions, we observed how the cross-correlation R varied with shifts in signal alignment. Significant interactions are indicated by a notable deviation of the cross-correlation peak from the background level. Figs. 2(A-F) illustrate this: synchronized signals (A,C) demonstrate a marked decay in $R(\tau)$ (E), while non-synchronized signals (B,D) do not show such decay (F).

For a quantitative measure of correlation significance, we introduced a Z-score-like index 'w', representing the deviation of the maximal cross-correlation value (R_{max}, detected at a specific time shift τ^*) from the mean, normalized by the standard deviation of $R(\tau)$. The index w thus quantifies the extent to which R_{max} stands out from the background, as shown in Fig. 2(E). The formula is expressed as:

$$w^{i,j} = \frac{(|R_{max}| - \langle R \rangle)}{\sigma(R)} \tag{1}$$

where $\langle R \rangle$ and $\sigma(R)$ denote the mean and standard deviation of $R(\tau)$, respectively.

A larger w indicates a more significant coupling between signals x and y. Conversely, a lower w suggests a non-significant interaction. To further validate significant connections, we compared cross-correlations of simultaneous signals from different locations against those from distinct time points, expected to be non-synchronized. As shown in Fig. 2(G), analysis of 10,000 signal pairs revealed that surrogate data typically yielded low w values, while real data could reach higher values, indicative of true synchronization.

High w values for real data, typically found for small shifts τ^*, corroborate with the rapid propagation of brain waves [32, 33].

In setting our analysis parameters, particularly $w > 4.5$ and $|\tau| < 0.05$s, we based our criteria on empirical benchmarks and comparative analysis with surrogate data. The choice of $w > 4.5$ was influenced by our observation that the highest 'w' values for random links in the surrogate data is around 4, which we deemed representative of false coupling. Thus, we established $w > 4.5$ as a conservative threshold to ensure the identification of true synaptic coupling rather than artifacts.

The parameter τ was set based on the distribution of τ values in the surrogate data, which exhibits uniform distribution, contrasting with the authentic data that exhibited τ values up to 0.05,

as discerned in Fig. 2(H). This observation guided the establishment of $\tau < 0.05$s as a reasonable upper bound for detecting meaningful interactions.

Furthermore, we calibrated 'w' and τ to ensure that the fraction of real links identified under these constraints approximated 0.02 of the total potential links. This approach was chosen to improve the accuracy in detecting real neural connections, while also decreasing the chances of mistakenly identifying non-existent connections.

High 'w' values for actual data, typically associated with small shifts in τ^*, align with the fast propagation of brain waves, supporting their significance in neural communication. We consider interactions with $\tau^* \in [-0.05, 0.05]$ seconds and $w > 4.5$ as significant, where the fraction of such links at each site are summarized in Table 2.

It's important to consider how the frequency of a signal affects the calculated parameters, especially 'w'. The main frequency that matches between signals largely determines the highest point of the cross-correlation function, which in turn influences the calculation of 'w'. However, the importance of 'w' doesn't depend only on the frequency's numerical value. Rather, 'w' acts similarly to a Z-score, evaluating the maximum point of cross-correlation in relation to the standard deviation of the cross-correlation. This method ensures that the assessment of 'w' more accurately represents the strength of the correlation with respect to level of noise, instead of being overly affected by the signals' absolute frequency. This approach makes sure that our method remains equally sensitive to signal correlations, no matter the frequency range of the signals being analyzed.

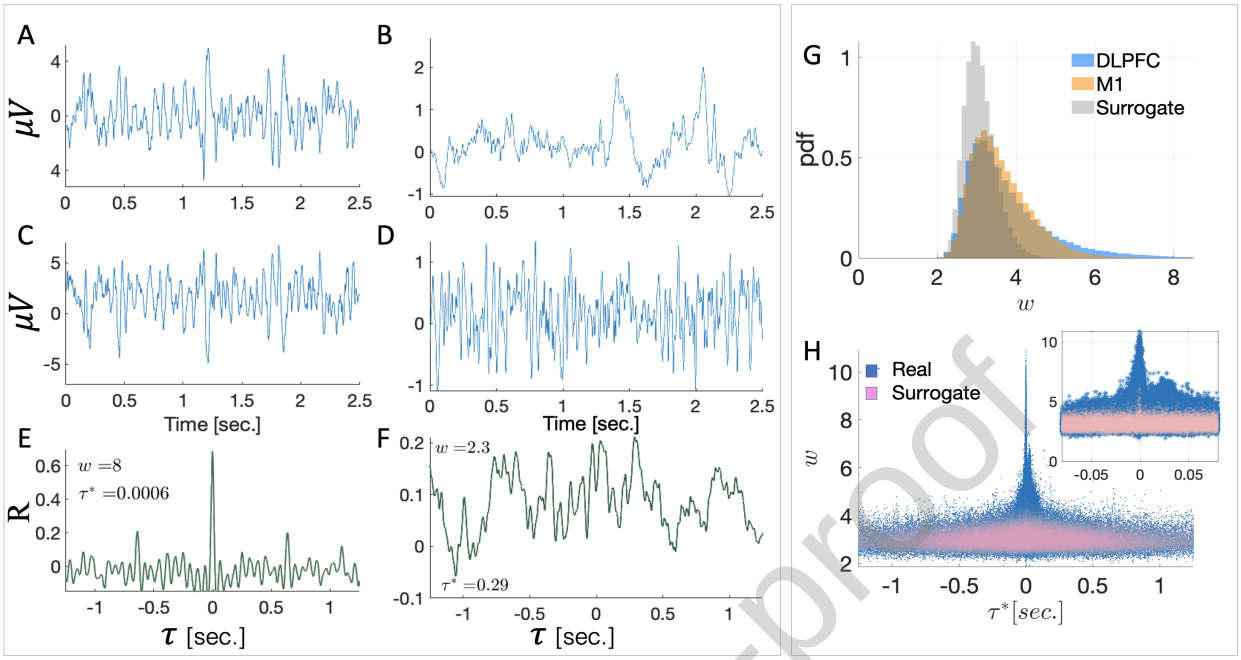

Figure 2: **Analysis of Significant Neural Interactions via Cross-Correlation and Surrogate Methods. A-F,** Demonstration of two pairs of signals (blue curves in panels A and C from the cortex [Ctx], and panels B and D from the globus pallidus [Gp]), following the application of a [1-80Hz] low-pass filter to the raw LFP data. **E-F**, Exhibit the cross-correlation index R with respect to the temporal shift τ between signal pairs A-C and B-D, respectively. Signals A and C show a pronounced peak in R at $\tau^* = \tau|_{R(\tau)\equiv R_{\max}} = 0$, and a rapid decay of $R(\tau)$ for $|\tau| > 0$. In contrast, signals B and D, as shown in F, demonstrate a variable $R(\tau)$ without a distinct peak or decay pattern, signifying no correlation. The significance metric w evaluates $R(\tau)$ by normalizing $R_{\max}$ with the mean and standard deviation of $R(\tau)$ (see Eq. 1). Consequently, a greater w value is observed in E ($w = 8$) than in F ($w = 2.3$). **G,** Depicts the w distribution for all analyzed data versus surrogate signals. Surrogate signals, selected randomly from different electrodes, nuclei, and time points, display a generally lower w distribution compared to real signals, with the maximum w for surrogates around 4. Panel **H** indicates that the highest w values for real data occur near $\tau^* \approx 0$. This scatter plot visualizes 10,000 instances of w versus τ^* for real (blue dots) and surrogate data (red dots). Notably, real signals correspond to simultaneous deep and cortical recordings, whereas surrogate pairs are randomly matched. This results in higher w values for real data around $\tau^* \approx 0$, unlike the uniform distribution observed in surrogates. An inset offers a detailed view of the $\tau^* \in [-0.08 - 0.08]$ range.

Location	Ctx	Str	Gp	Ic	Stn
M1	0.08	0.14	0.14	0.13	0.08
DLPFC	0.51	0.24	0.09	0.24	0.04

Table 2: **Proportion of Significant Neural Links Across Nuclei and Cortical Areas.** This table presents the proportion of significant neural interactions for each brain region. These proportions were derived by calculating the ratio of the count of significant links to the total number of analyzed time windows at each location. A link was deemed significant if it met the criteria of $\tau^* \in [-0.05; 0.05]$ seconds and $w > 4.5$.

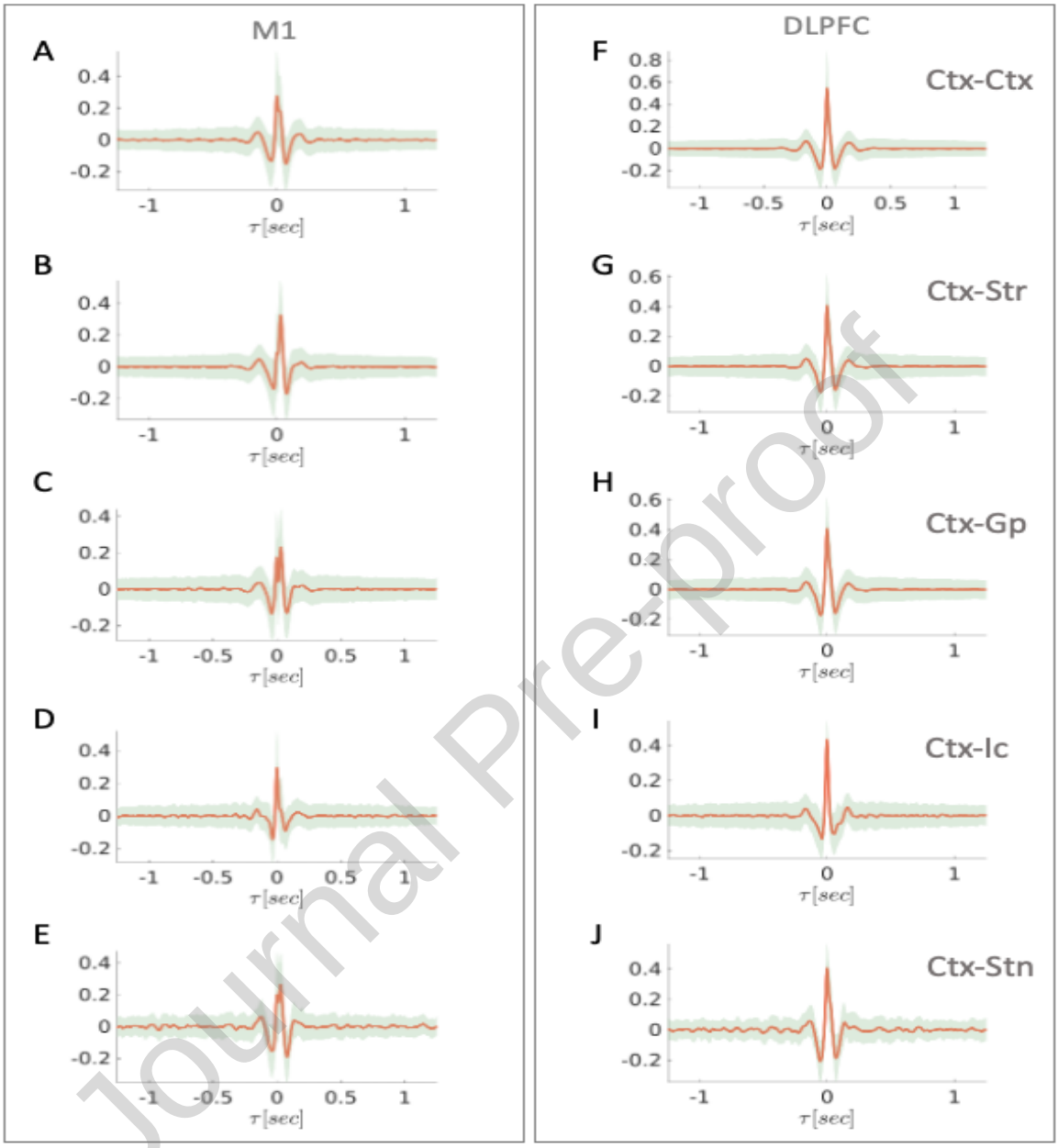

Figure 3: **Cross-correlations.** The cross-correlations of the M1 and DLPFC electrodes with the deep electrode located at the DLPFC and at the BG nuclei. Left column (A - E) shows the cross-correlations between DLPFC-Ctx, DLPFC-Str, DLPFC-Gp, DLPFC-Ic and DLPFC-Stn respectively. On the right column (F - J), we show the same interactions for the DLPFC - Ctx. Here, we show only correlations with $w > 4.5$ and $\tau^* < 0.05$ sec., of the time windows that were analyzed. In red is the mean, and the shaded green area represents the standard deviation.

3. Results

Correlation Analysis, Score Evaluation, and τ^* Distributions. Our analysis revealed that only a subset of the cross-correlations exhibited synchronization, resulting in significant linkages, as detailed in Table 2. Specifically, for DLPFC-BG pairs, the percentage of significant links ranged from 8% to 14%, whereas for M1-BG pairs, this range was broader, from 4% to 51%. The nature of these significant cross-correlations is graphically depicted in Fig. 3.

The time delay τ^* at which $R(\tau)$ peaks is indicative of the interaction direction between signal pairs x and y. A positive τ^* suggests an interaction initiating in the cortex and propagating towards the basal ganglia, while a negative τ^* indicates the reverse. Fig. 4, panels A-J, display a bi-modal distribution of time delays for both cortical regions. However, the BG-DLPFC interactions (right panels of Fig. 4) are predominantly characterized by the first mode ($\tau^* \sim 0$), whereas BG-M1 interactions (left panels) show significant representation in both modes. Nonetheless, the average τ^* for significant real links (with $w > 4.5$) are similar for both M1 and DLPFC, as seen in Fig. 4, panels K-L.

Duration of Significant Neural Links. To ascertain the duration or "lifetime" of a significant link, we divided each 120-second recording at each site into overlapping 2.5-second windows. A link was considered significant in a given window if $w > 4.5$ and $|\tau^*| < 0.05$ seconds. The cumulative duration of these links was then calculated by summing the successive windows wherein the link persisted. Fig. 5 illustrates the lifespan distribution of these interactions across various nuclei. Notably, as the probe progresses deeper, the duration of the links tends to decrease. The longest peak durations were observed in upper area links, specifically 20 seconds for M1-DLPFC and 100 seconds for DLPFC-DLPFC links. The M1-Str and DLPFC-Str connections lasted around 25 and 30 seconds, respectively, while both M1-GP and DLPFC-GP links had durations close to 20 seconds. The shortest durations, around 10 seconds, were found in the Ic links and both M1/DLPFC - Stn links.

Modes Analysis. The bi-modal distribution of τ^* in Fig. 4 is particularly pronounced in M1-GP links, supporting the hypothesis of dual transfer mechanisms. The DLPFC-GP links predominantly exhibit zero time lag (right panels), suggesting volume conduction, whereas the M1-GP paths (left panels) show a more balanced distribution, indicating a potential synaptic information transfer mechanism for the second mode, typically around 30 milliseconds.

To further validate the existence of two distinct transfer mechanisms, we analyzed the composition of link sequences, or sub-links. These were categorized into two regimes based on the distribution intersection point in Fig. 4. Each sub-link was classified as '1' if its τ^* fell in the first regime and as '2' for the second regime. Interestingly, most links comprised either consecutive '1's or '2's, suggesting a dominance of one transfer mechanism per interaction. This is visually represented in Fig. 6. The first mode, predominantly with $\tau^* \sim 0$, likely corresponds to volume conduction, aligning with the propagation speed of bio-electromagnetic waves. The second mode, with $\tau^* \sim 0.03$ seconds, appears to represent slower information transfer along axons and

synapses. Fig. 7 indicates that mixed-mode sequences (e.g., ‘1,2,1’) are rare, further corroborating our hypothesis of dual transfer mechanisms.

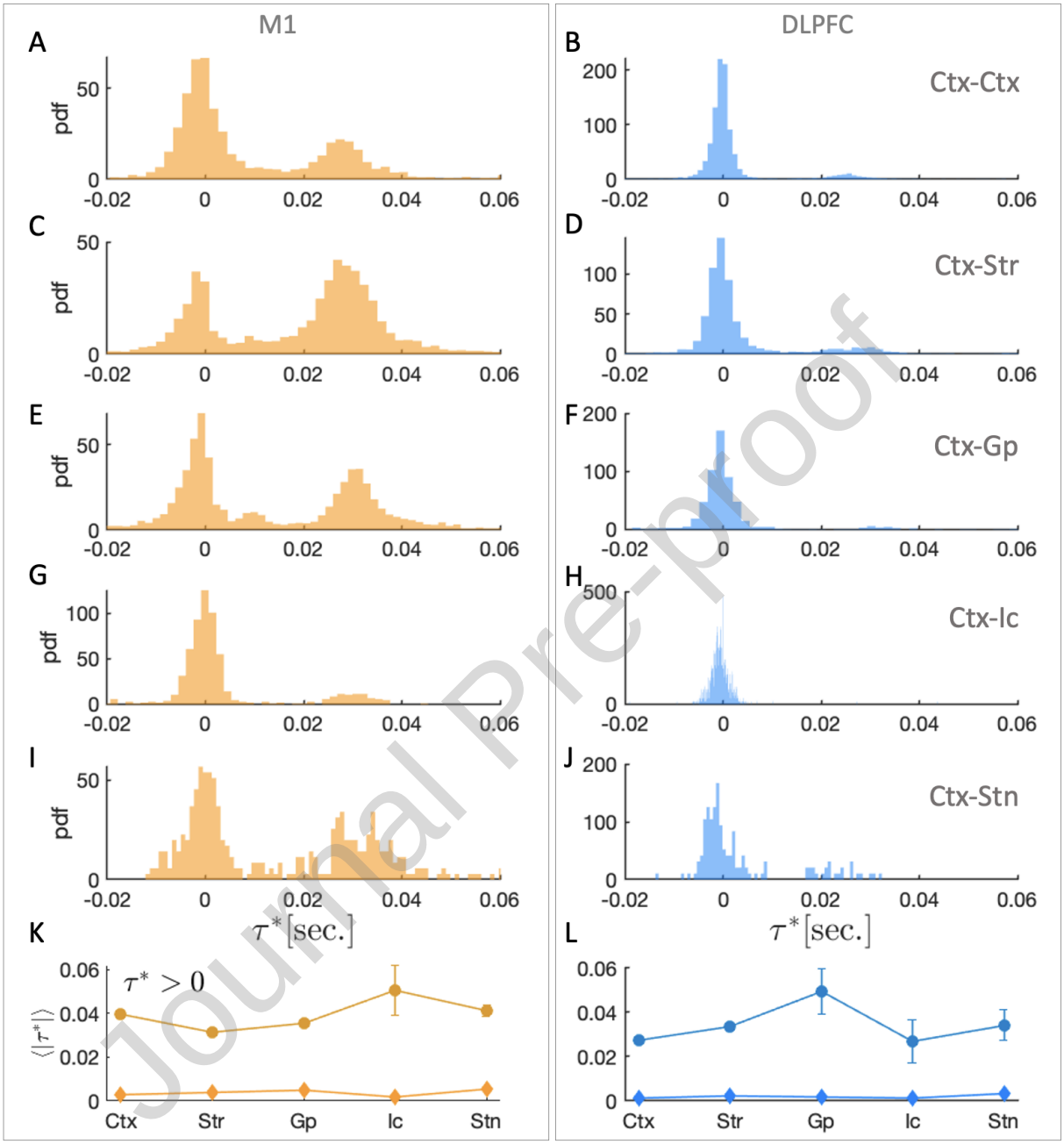

Figure 4: **Analysis of Time Delays and τ^* Distribution in Basal Ganglia-Cerebral Cortex Interactions. A-J** Display the τ^* distribution for all interactions between the cerebral cortex and basal ganglia (BG) nuclei. The left and right columns represent the M1-BG and DLPFC-BG links, respectively. Notably, these distributions are bi-modal, indicating the presence of two distinct types of links. The separation between the first and second mode distributions was manually determined using the minimal point of an estimated function, with $\tau^* = 0.01$ seconds selected as the threshold for all distributions. **K-L,** Illustrate the average τ^* values for the nuclei, focusing on interactions where $\tau^* > 0$. This highlights the mean time delays between signals from the M1, DLPFC, and the moving electrode. A positive τ^* implies that the signal was initiated or detected earlier in the cortex, accounting for 80% of the significant links. Diamonds and circles represent the average time delays for the first and second modes, respectively.

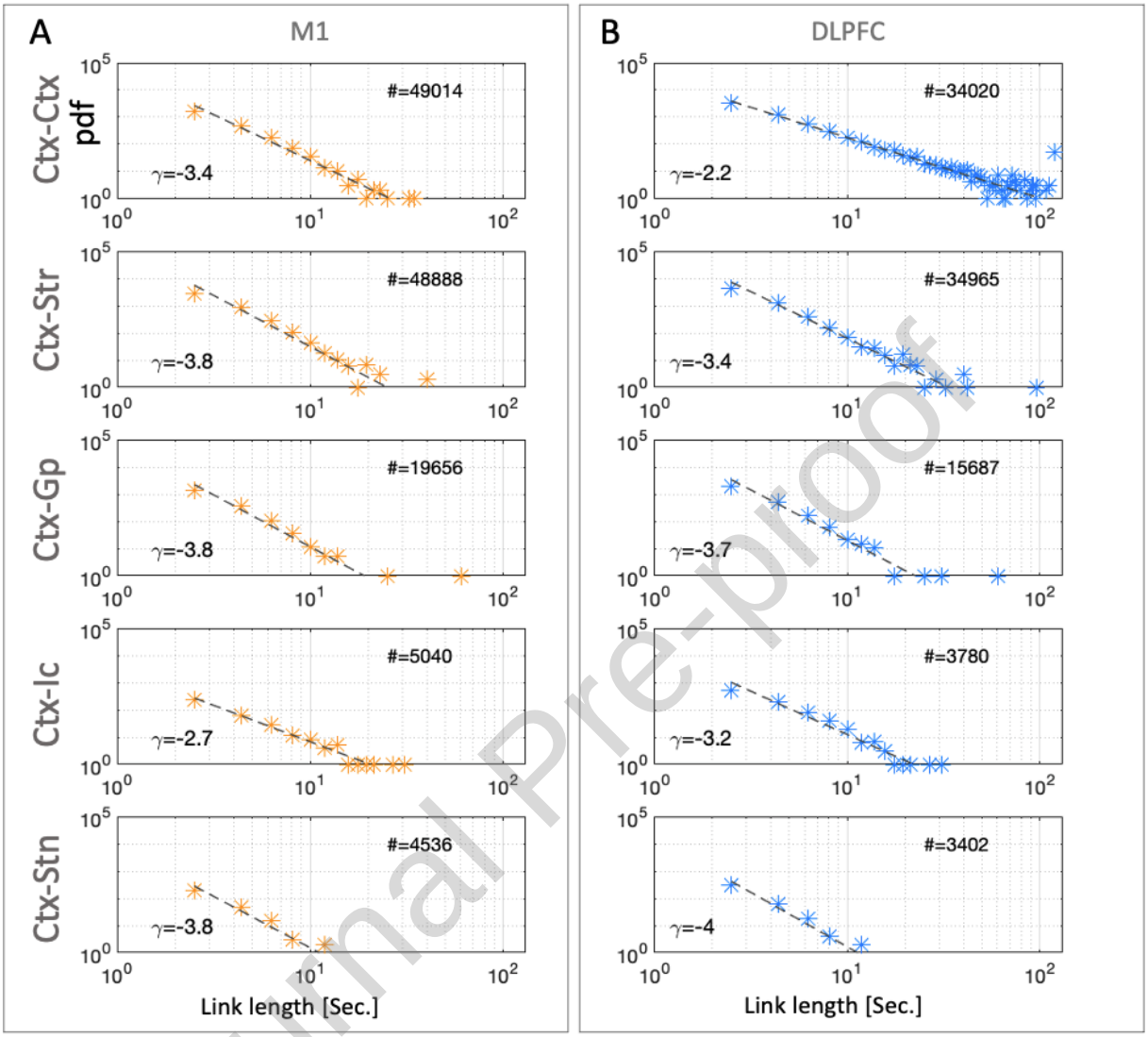

Figure 5: **Duration Distribution of Neural Links Across Different Loci.** The left and right columns depict the probability density functions (PDFs) of link durations for the M1 and DLPFC electrode sets, respectively. Each 120-second recording is divided into overlapping 2.5-second windows with a 25% overlap (0.625 seconds). For each window, we assess the cross-correlation between signals from the deep electrode and the corresponding cortical electrode, calculating w. A link is considered significant if $w > 4.5$ and $\tau^* < 0.05$ seconds. The graph illustrates the duration of consecutive significant sub-links formed with cortical electrodes at various recording sites. Presented in a log-log scale, the data suggest a power-law distribution for the survival time of the links, with the exponent γ provided. Notably, the decline in significant link duration is more pronounced for deeper nuclei. Additionally, for most nuclei, link durations tend to be longer for the DLPFC frontal lobe electrode set compared to the M1 set, indicating a possible influence of spatial distance on LFP signal duration. The exponents exhibit a consistent increase with depth, except for the internal capsule (Ic), characterized by white matter where signals might propagate more rapidly.

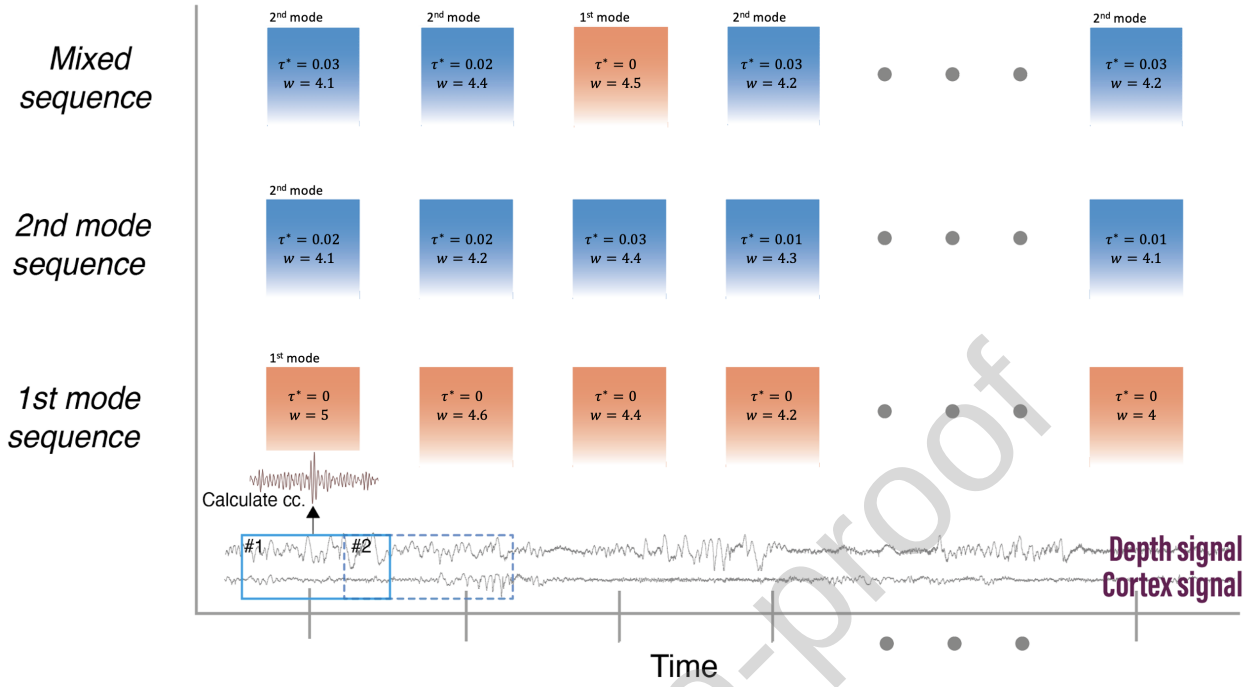

Figure 6: **Characterization of Modes Sequences Based on τ^*.** This figure is segmented into three main rows, plus an additional bottom row, illustrating the composition of sequences in both cortical and deep signals. The upper row depicts a mixed mode sequence with variable τ^* values (e.g., sequences like 2,2,1,2,... in sub-links). The middle row shows a sequence comprised entirely of the second mode (sub-links of 2,2,2,...), and the lower row portrays a sequence exclusively in the first mode (1,1,1,...), where each τ^* equals 0. Each sequence spans n time-windows of 2.5 seconds (sub-links), with each window satisfying the condition $w > 4.5$, indicating significant cross-correlation. For every sequence of length n, τ^* for each time window (sub-link) is calculated, and the sequence is classified as either predominantly first or second mode based on these τ^* values.

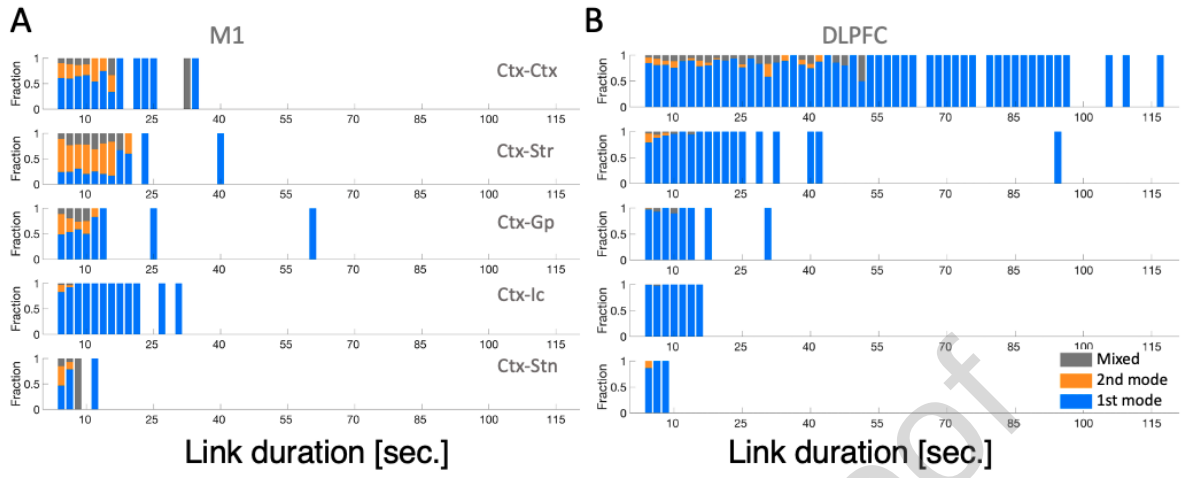

Figure 7: **Analysis of Sequence Mode Compositions in Neural Links.** **A,** Examines the sequence compositions formed between M1 electrodes and the deep electrode. **B,** Focuses on the sequence compositions involving DLPFC electrodes and the deep electrode. Each link, with a duration of time length L, is dissected into 2.5-second sub-links. The τ^* values of these sub-links are analyzed to determine if they fall within the range of the first or second mode, as shown in Fig. 4. Our findings reveal that most sequences predominantly belong to either the first or the second mode, with a minimal fraction displaying a mix of both modes. Sequences comprised entirely of τ^* values from the first (or second) mode are termed "first (or second) mode" sequences. If a sequence includes a blend of both modes, it is classified as a "mixed" sequence. Notably, the frontal cortex links (right panel) primarily exhibit first mode sequences with $\langle\tau\rangle \backsimeq 0$, whereas second mode sequences with $\langle\tau\rangle \backsimeq 0.03$ are more prevalent in M1 links. Additionally, for the internal capsule (Ic), which is composed of white matter, the majority of links are first mode in both the frontal cortex and M1.

4. Summary and Discussion

We have uncovered novel synchronization properties in local field potentials (LFPs) linking the cerebral cortex (M1 and DLPFC) with basal ganglia (BG) structures (striatum, globus pallidus, internal capsule, and subthalamic nucleus). These discoveries shed light on the longstanding debate regarding whether BG LFPs primarily reflect volume conduction or synaptic input (information flow). We introduced a novel cross-correlation method to identify significant links and established a pattern for the duration of these links. Our analysis involved LFPs in the [1,80] Hz range, recorded via micro-electrodes in the deep layers of the cerebral cortex (M1 and DLPFC), along with a moving electrode in the basal ganglia. All recordings were conducted with an alert primate, not engaged in behavioral tasks.

Our findings suggest that LFP signals comprise two distinct mechanisms: synaptic inputs and volume conduction. Segmenting the 120-second recordings into overlapping 2.5-second windows, we identified a fraction of highly correlated windows (defined by link strength $w > 4.5$ and

$\tau^* \in [-0.05, 0.05]$). Significant links range from 8% to 14% in M1-BG pairs and from 4% to 51% in DLPFC-BG pairs, as shown in Table 2. The temporal delay in cross-correlation, as depicted in Fig. 4, indicates two modes of interaction: a short delay for volume conductance and a longer delay for synaptic input-based information transfer. While most links are predominantly in one mode, a small fraction exhibit a mixture of both, indicating the complexity of neural interactions.

4.1. Differences in LFP Links Between M1, DLPFC, and BG

The cross-correlation links between M1-BG and DLPFC-BG display distinct properties. M1-BG pairs are characterized by more functional links with non-zero-time delays, supporting the basal ganglia's involvement in functionally segregated circuits linked to both motor and non-motor areas of the cerebral cortex. This is consistent with previous studies highlighting the basal ganglia's role in motor functionalities [34, 35].

We observed variations in the τ^* distributions and minor changes in their averages. These observations that the value of τ^* remains relatively constant at approximately 0.03 seconds throughout the basal ganglia circuits see Fig. 4 are surprising and counter-intuitive. A plausible explanation could be by the intricate interplay of direct "shortcut" synaptic projections, like thalamic-cortical-GPi connections and the Stn, which directly receives signals from the cerebral cortex. Simultaneously, there are also indirect pathways linking Basal Ganglia nuclei network with the cerebral cortex. This complexity involves the Stn, primarily getting signals from the cerebral cortex (direct projection) and the GPe, projecting to both segments of the Globus Pallidus (GPe, GPi) [36]. These "shortcuts" might superimpose with the time delay of the indirect pathway, potentially explaining the broad distribution of the time delay around 0.03 seconds. This architecture minimizes the impact of physical distance on time delays. Our analysis indicates that synaptic delay may not necessarily correlate linearly with the physical distance between regions. Rather, it might be influenced by the number of synaptic connections involved in the transmission pathway, see e.g., [37].

In terms of link durations, deeper nuclei showed shorter durations, and DLPFC-BG links were longer than M1-BG links (Fig. 5). This trend might be due to the greater distances and higher number of synapses in deeper connections, leading to increased noise and signal decay. The duration of these links—conceptualized as the continuous cross-correlation between two nuclei—can be analogous to the sustained conversation or information transfer between them, highlighting the period during which the coupling remains uninterrupted during data recording.

Figures 5, 6, and 7 elucidate the duration of links associated with volume conduction, time-delayed cross-correlation of the second mode, and mixed durations. The persistence of these links could change under pathological conditions, such as Parkinson's disease (PD), and might serve as an additional indicator of the disease's severity, warranting further investigation.

The two primary modes in τ^* distributions suggest different interaction mechanisms: short delays for volume conductance and longer delays for synaptic input-based information transfer.

Notably, frontal cortex-deep electrode links mainly consisted of first mode sequences, whereas M1-BG links exhibited a higher presence of second mode sequences, suggesting differential functional dynamics in these pathways.

Our methodology and findings pave the way for differentiating between volume conduction interactions and actual information flow, addressing a crucial question in neuroscience [38–40]. Future research could explore whether second mode links convey more information than those associated with volume conductance. Additionally, the study of LFP signals could advance DBS research, especially in developing adaptive protocols.

In the context of PD, characterized by beta-pathophysiological oscillations [41], We suggest that synaptic inputs (time delay information flow dependence) would remain or rather increase (as happens for inhibitory projections) during PD or other pathological states. This capability could be crucial for future closed-loop DBS, potentially aiding in differentiating between possible spurious PD beta-band oscillations attributed to volume conduction and authentic synaptic beta-band (neuronal) oscillations.

In the supplementary information of the revised manuscript, see Fig. 10, we have extended our analysis to include different brain wave ranges, such as alpha, beta, and gamma band activities. Although some irregularities were observed within the beta band W distribution, a comprehensive exploration of PD-related LFP changes was beyond the scope of our current study and demands targeted research in PD models.

Our framework suggests avenues for future DBS research and applications, including the exploration of the closed-loop implementation of BG-Cortex LFP-based and adaptive DBS protocols [40]. Further research is required, particularly involving data from Parkinsonian models, is necessary to fully comprehend the alterations in LFPs associated with PD and to apply our methodology effectively in such contexts

Moreover, the greater abundance of synaptic inputs within M1-BG links, compared to DLPFC-BG, does not imply exclusivity of synaptic circuits in M1-BG or solely volume conduction in DLPFC-BG. We do observe the existence of synaptic input links between DLPFC-BG and M1-BG; however, the number of synaptic input links is much fewer between DLPFC-BG compared to M1-BG. Figure 7 presents the histograms of these links, categorized into three types: (1) Volume conduction links with no time delay, as we assume that volume conduction follows the dispersion rules of Maxwell's equations, where the distribution velocity depends on the dielectric (brain tissue) conductivity, and the time delay should be approximately zero; (2) Synaptic inputs with a time delay, representing signal transformation delayed by synaptic connections; and (3) Mixed connections (both volume conduction and synaptic inputs realizations). The figure illustrates that consistent with our claim above, M1-BG exhibits a significantly higher prevalence of synaptic inputs compared to DLPFC-BG. Additionally, we observe mixed connections in the latter. This nuanced view underscores the complexity of neural interactions and the presence of both mechanisms in different brain regions, enhancing our understanding of neural circuitry and its implications in neurodegenerative diseases and therapeutic interventions.

Acknowledgments

No acknowledgments.

Funding

Nothing to declare.

Credit authorship contribution statement

EEA discussed, implemented the methodologies, performed the analysis, prepared the figures. SM and RM helped in collecting the data. SH and HB supervised the project. SM conceptualized, developed, and supervised the project, initiated, and designed the experiments with HB, and collected the data. SM, EEA, SH, and HB wrote the manuscript. All authors discussed the results, reviewed the manuscript, and made their comments.

Statement of Ethics

All procedures were conducted in accordance with the Hebrew University guidelines for animal care and the National Institute of Health Guide for the Care and Use of Laboratory Animals. The Hebrew University is an AAALAC (Association for Assessment and Accreditation of Laboratory Animal Care) approved institute.

Declaration of Competing Interest

The authors declare that they have no known competing financial interests or personal relationships that could have appeared to influence the work reported in this paper.

References

[1] György Buzsáki, Costas A Anastassiou, and Christof Koch. The origin of extracellular fields and currents—eeg, ecog, lfp and spikes. *Nature reviews neuroscience*, 13(6):407–420, 2012.

[2] Klaus Wimmer, Marc Ramon, Tatiana Pasternak, and Albert Compte. Transitions between multiband oscillatory patterns characterize memory-guided perceptual decisions in prefrontal circuits. *Journal of Neuroscience*, 36(2):489–505, 2016.

[3] Alik S Widge, Sarah R Heilbronner, and Benjamin Y Hayden. Prefrontal cortex and cognitive control: new insights from human electrophysiology. *F1000Research*, 8, 2019.

[4] J Andrew Henrie and Robert Shapley. Lfp power spectra in v1 cortex: the graded effect of stimulus contrast. *Journal of neurophysiology*, 94(1):479–490, 2005.

[5] Conrado A Bosman, Jan-Mathijs Schoffelen, Nicolas Brunet, Robert Oostenveld, Andre M Bastos, Thilo Womelsdorf, Birthe Rubehn, Thomas Stieglitz, Peter De Weerd, and Pascal Fries. Attentional stimulus selection through selective synchronization between monkey visual areas. *Neuron*, 75(5):875–888, 2012.

[6] James E Carmichael, Jimmie M Gmaz, and Matthijs AA van der Meer. Gamma oscillations in the rat ventral striatum originate in the piriform cortex. *Journal of Neuroscience*, 37(33):7962–7974, 2017.

[7] Andrew Jackson and Thomas M Hall. Decoding local field potentials for neural interfaces. *IEEE Transactions on Neural Systems and Rehabilitation Engineering*, 25(10):1705–1714, 2016.

[8] Klaus-Robert Müller, Michael Tangermann, Guido Dornhege, Matthias Krauledat, Gabriel Curio, and Benjamin Blankertz. Machine learning for real-time single-trial eeg-analysis: from brain–computer interfacing to mental state monitoring. *Journal of neuroscience methods*, 167(1):82–90, 2008.

[9] JF Marsden, P Limousin-Dowsey, P Ashby, P Pollak, and P Brown. Subthalamic nucleus, sensorimotor cortex and muscle interrelationships in parkinson's disease. *Brain*, 124(2):378–388, 2001.

[10] John P Donoghue, Jerome N Sanes, Nicholas G Hatsopoulos, and Gyongi Gaal. Neural discharge and local field potential oscillations in primate motor cortex during voluntary movements. *Journal of neurophysiology*, 79(1):159–173, 1998.

[11] Maria C Rodriguez-Oroz, Manuel Rodriguez, Jorge Guridi, Klaus Mewes, Vijay Chockkman, Jerrold Vitek, Mahlon R DeLong, and Jose A Obeso. The subthalamic nucleus in parkinson's disease: somatotopic organization and physiological characteristics. *Brain*, 124(9):1777–1790, 2001.

[12] Shay Moshel, Reuben Ruby Shamir, Aeyal Raz, Fernando Ramirez de Noriega, Renana Eitan, Hagai Bergman, and Zvi Israel. Subthalamic nucleus long-range synchronization—an independent hallmark of human parkinson's disease. *Frontiers in systems neuroscience*, 7:79, 2013.

[13] Maya Slovik, Boris Rosin, Shay Moshel, Rea Mitelman, Eitan Schechtman, Renana Eitan, Aeyal Raz, and Hagai Bergman. Ketamine induced converged synchronous gamma oscillations in the cortico-basal ganglia network of nonhuman primates. *Journal of neurophysiology*, 118(2):917–931, 2017.

[14] Musa Ozturk, Ashwin Viswanathan, Sameer A Sheth, and Nuri F Ince. Electroceutically induced subthalamic high-frequency oscillations and evoked compound activity may explain the mechanism of therapeutic stimulation in parkinson's disease. *Communications biology*, 4(1):1–14, 2021.

[15] Shlomit Yuval-Greenberg, Orr Tomer, Alon S Keren, Israel Nelken, and Leon Y Deouell.

Transient induced gamma-band response in eeg as a manifestation of miniature saccades. *Neuron*, 58(3):429–441, 2008.

[16] Peter Brown and David Williams. Basal ganglia local field potential activity: character and functional significance in the human. *Clinical neurophysiology*, 116(11):2510–2519, 2005.

[17] Constance Hammond, Hagai Bergman, and Peter Brown. Pathological synchronization in parkinson's disease: networks, models and treatments. *Trends in neurosciences*, 30(7):357–364, 2007.

[18] Tolga Esat Özkurt, Markus Butz, Melanie Homburger, Saskia Elben, Jan Vesper, Lars Wojtecki, and Alfons Schnitzler. High frequency oscillations in the subthalamic nucleus: a neurophysiological marker of the motor state in parkinson's disease. *Experimental neurology*, 229(2):324–331, 2011.

[19] Andrei Belitski, Stefano Panzeri, Cesare Magri, Nikos K Logothetis, and Christoph Kayser. Sensory information in local field potentials and spikes from visual and auditory cortices: time scales and frequency bands. *Journal of computational neuroscience*, 29(3):533–545, 2010.

[20] Wen-Ju Pan, Garth Thompson, Matthew Magnuson, Waqas Majeed, Dieter Jaeger, and Shella Keilholz. Broadband local field potentials correlate with spontaneous fluctuations in functional magnetic resonance imaging signals in the rat somatosensory cortex under isoflurane anesthesia. *Brain connectivity*, 1(2):119–131, 2011.

[21] Dora Hermes, Mai Nguyen, and Jonathan Winawer. Neuronal synchrony and the relation between the blood-oxygen-level dependent response and the local field potential. *PLoS biology*, 15(7):e2001461, 2017.

[22] Alexander Maier, Christopher J Aura, and David A Leopold. Infragranular sources of sustained local field potential responses in macaque primary visual cortex. *Journal of Neuroscience*, 31(6):1971–1980, 2011.

[23] Scott F Lempka and Cameron C McIntyre. Theoretical analysis of the local field potential in deep brain stimulation applications. *PloS one*, 8(3):e59839, 2013.

[24] Michael Okun, Amir Naim, and Ilan Lampl. The subthreshold relation between cortical local field potential and neuronal firing unveiled by intracellular recordings in awake rats. *Journal of neuroscience*, 30(12):4440–4448, 2010.

[25] Henrik Lindén, Klas H Pettersen, and Gaute T Einevoll. Intrinsic dendritic filtering gives low-pass power spectra of local field potentials. *Journal of computational neuroscience*, 29(3):423–444, 2010.

[26] Craig E Tenke and Jürgen Kayser. Generator localization by current source density (csd): implications of volume conduction and field closure at intracranial and scalp resolutions. *Clinical neurophysiology*, 123(12):2328–2345, 2012.

[27] Ana Parabucki and Ilan Lampl. Volume conduction coupling of whisker-evoked cortical lfp in the mouse olfactory bulb. *Cell reports*, 21(4):919–925, 2017.

[28] Gaute T Einevoll, Christoph Kayser, Nikos K Logothetis, and Stefano Panzeri. Modelling and analysis of local field potentials for studying the function of cortical circuits. *Nature Reviews Neuroscience*, 14(11):770–785, 2013.

[29] Laetitia Lalla, Pavel E Rueda Orozco, Maria-Teresa Jurado-Parras, Andrea Brovelli, and David Robbe. Local or not local: investigating the nature of striatal theta oscillations in behaving rats. *eneuro*, 4(5), 2017.

[30] CM Contreras, G Mexicano, and C Guzman-Flores. A stereotaxic brain atlas of the green monkey (cercopithecus aethiops aethiops). *Boletin de estudios medicos y biologicos*, 31(7-8):383–428, 1981.

[31] Svjetlana Miocinovic, Jianyu Zhang, Weidong Xu, Gary S Russo, Jerrold L Vitek, and Cameron C McIntyre. Stereotactic neurosurgical planning, recording, and visualization for deep brain stimulation in non-human primates. *Journal of neuroscience methods*, 162(1-2):32–41, 2007.

[32] Honghui Zhang, Andrew J Watrous, Ansh Patel, and Joshua Jacobs. Theta and alpha oscillations are traveling waves in the human neocortex. *Neuron*, 98(6):1269–1281, 2018.

[33] Tatsuo K Sato, Ian Nauhaus, and Matteo Carandini. Traveling waves in visual cortex. *Neuron*, 75(2):218–229, 2012.

[34] Suzanne N Haber. The primate basal ganglia: parallel and integrative networks. *Journal of chemical neuroanatomy*, 26(4):317–330, 2003.

[35] Andreea C Bostan, Richard P Dum, and Peter L Strick. Functional anatomy of basal ganglia circuits with the cerebral cortex and the cerebellum. *Current Concepts in Movement Disorder Management*, 33:50–61, 2018.

[36] Eva M Navarro-Lopez, Utku Çelikok, and Neslihan S Şengör. A dynamical model for the basal ganglia-thalamo-cortical oscillatory activity and its implications in parkinson's disease. *Cognitive Neurodynamics*, 15(4):693–720, 2021.

[37] Charles R. Gerfen and J. Paul Bolam. Chapter 1 - the neuroanatomical organization of the basal ganglia. In Heinz Steiner and Kuei Y. Tseng, editors, *Handbook of Basal Ganglia Structure and Function*, volume 20 of *Handbook of Behavioral Neuroscience*, pages 3–28. Elsevier, 2010.

[38] Felix Jung, Victoria Witte, Yevgenij Yanovsky, Matthias Klumpp, Jurij Brankačk, Adriano BL Tort, and Andreas Draguhn. Differential modulation of parietal cortex activity by respiration and θ oscillations. *Journal of Neurophysiology*, 127(3):801–817, 2022.

[39] Saed Khawaldeh, Gerd Tinkhauser, Flavie Torrecillos, Shenghong He, Thomas Foltynie, Patricia Limousin, Ludvic Zrinzo, Ashwini Oswal, Andrew J Quinn, Diego Vidaurre,

et al. Balance between competing spectral states in subthalamic nucleus is linked to motor impairment in parkinson's disease. *Brain*, 145(1):237–250, 2022.

[40] Tal Sharf, Tjitse van der Molen, Stella MK Glasauer, Elmer Guzman, Alessio P Buccino, Gabriel Luna, Zhuowei Cheng, Morgane Audouard, Kamalini G Ranasinghe, Kiwamu Kudo, et al. Functional neuronal circuitry and oscillatory dynamics in human brain organoids. *Nature communications*, 13(1):1–20, 2022.

[41] Ying Yu, David Escobar Sanabria, Jing Wang, Claudia M Hendrix, Jianyu Zhang, Shane D Nebeck, Alexia M Amundson, Zachary B Busby, Devyn L Bauer, Matthew D Johnson, et al. Parkinsonism alters beta burst dynamics across the basal ganglia–motor cortical network. *Journal of Neuroscience*, 41(10):2274–2286, 2021.

Declaration of Competing Interest

The authors declare that they have no known competing financial interests or personal relationships that could have appeared to influence the work reported in this paper.